

Cite this: *RSC Adv.*, 2016, 6, 106914

## Time-dependent evolution of the nitrogen configurations in N-doped graphene films†

Boitumelo J. Matsoso,<sup>ab</sup> Kamalakannan Ranganathan,<sup>ab</sup> Bridget K. Mutuma,<sup>ab</sup>  
Tsenolo Leretholi,<sup>b</sup> Glenn Jones<sup>cd</sup> and Neil J. Coville<sup>\*ab</sup>

Large-area time-controlled N-doped graphene films were grown on a Cu foil using an ammonia-assisted atmospheric pressure chemical vapour deposition (APCVD) technique. The films were characterized using optical microscopy, Raman spectroscopy and X-ray photoelectron spectroscopy (XPS). Raman spectroscopy was used to verify the doping level and lattice distortion in the graphene films, while the degree of N-doping (N/C at%) and nitrogen configuration were studied by XPS. The results showed that both total nitrogen content and configurations were strongly dependent on the growth time. Notably, at short growth time (2 min) pyridinic-rich films with high oxygen content (~47.02%) were produced, and the total N-content reached a maximum of 4.68%. Interestingly longer growth times (20 min) also resulted in pyridinic-rich films, however both the nitrogen and oxygen content were at lower values of 2.84% and ~26.07%, respectively. With increasing growth time, Raman spectra showed a decreasing doping level as seen by the decreasing  $I_D/I_G$  ratio values (1.2 to 0.9). Additionally, Raman peaks exhibited a systematic blue shift due to the compressive strain on the C–C bonds during the incorporation of N atoms into the graphene lattice. The study presents an in-depth understanding of how exposure time of N-dopants influences the bonding states of nitrogen atoms to carbon atoms, thereby dictating the resulting type of N-configurations as well as the overall nitrogen content.

Received 28th September 2016  
Accepted 27th October 2016

DOI: 10.1039/c6ra24094a

www.rsc.org/advances

### 1. Introduction

Graphene, a two dimensional (2D) crystalline allotrope of carbon,<sup>1</sup> has attracted great interest for applications in the field of energy and storage devices due to its unique properties.<sup>1–3</sup> These unique properties include high chemical stability, high electrical conductivity, and large surface area;<sup>1,4–10</sup> thereby enabling graphene to have potential applications in supercapacitors, photovoltaics, sensors, electronics, or Li batteries.<sup>11–14</sup> However, being a zero band gap 2D material,<sup>2,15</sup> graphene is not ready for its application in the next generation electronic devices because its electrical conductivity cannot be completely controlled when compared with classical semiconductors (such as silicon, germanium, gallium arsenide, silicon carbide, *etc.*). Reports have however shown that graphene can compete with commercial semiconductors if its

electrochemical properties are tuned. This can be achieved by either functionalization of the surface of graphene with gaseous molecules, metals, organic molecules, or by the chemical substitution of foreign atoms into the graphene lattice.<sup>16–19</sup> Theoretical and experimental attempts have indicated that chemical doping of graphene with heteroatoms is the most efficient technique for tailoring the electronic, chemical, optical and magnetic properties of graphene;<sup>20–22</sup> to broaden its applications. Doping with heteroatoms, such as nitrogen, phosphorus, sulphur, nitrogen/sulphur, or nitrogen/boron, allows graphene to have an open band gap; hence leading to the transformation of graphene into a p- or n-type semiconductor.<sup>23,24</sup> It has been shown that the chemical doping influences the properties of graphene according to the at least two features of the dopant element, namely: (1) size of the dopant, and (2) dopant atom electronegativity.<sup>24</sup> These features play a significant role in determining the application of the doped graphene as well as in choosing the appropriate dopant.

Recent success in N-atom doping of carbon nanotubes (CNTs) to give N-CNTs<sup>25</sup> by chemical vapour deposition (CVD), arc discharge, and ammonia post-treatment techniques has encouraged attempts for the chemical N-doping of graphene films. This is because nitrogen (65 pm) has a comparable atomic size to that of C (70 pm), thus making its incorporation into the graphene lattice possible. Additionally, nitrogen has an extra electron in its outer shell, which plays a significant role in

<sup>a</sup>DST-NRF Centre of Excellence in Strong Materials, University of the Witwatersrand, Johannesburg, 2050, South Africa. E-mail: neil.coville@wits.ac.za; Fax: +27 11 717 6749

<sup>b</sup>Molecular Sciences Institute, School of Chemistry, University of the Witwatersrand, Johannesburg, 2050, South Africa

<sup>c</sup>Department of Chemistry, University College London, Gordon Street, London, UK

<sup>d</sup>Johnson Matthey Research Center, Building 22, CSIR Campus, Meiring Naude Road, Brummeria, Pretoria, 0184, South Africa

† Electronic supplementary information (ESI) available. See DOI: 10.1039/c6ra24094a



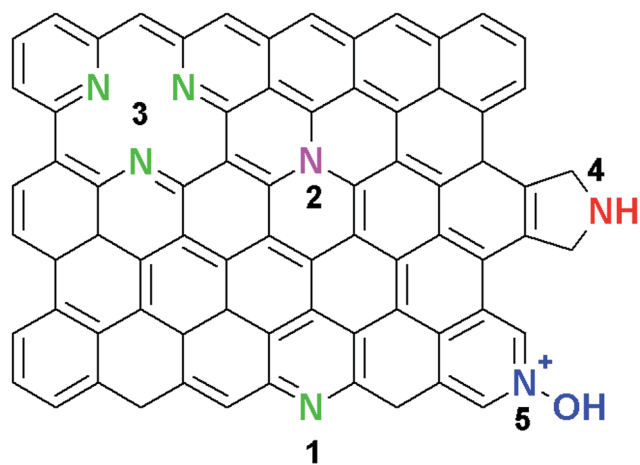
predicting the applications of the N-doped graphene by either inducing n- or p-type semiconducting behaviour.<sup>24</sup> Typically, in most reports on synthesized N-doped graphene, X-ray photoelectron spectroscopy (XPS) studies have shown that N atoms can be bonded to the C atoms in graphene in at least four bonding configurations (Scheme 1).

The bonding configurations are as follows: pyridinic-N (398.1–398.3 eV), pyrrolic-N (399.8–400.2 eV), quaternary or graphitic-N (401.1–402.7 eV), and oxidised pyridinic-N (403–405 eV).<sup>14,22,25–27</sup> Pyridinic-N is bonded to two C atoms at the edges of the graphene domains. Due to its  $sp^2$ -hybridisation, the pyridinic-N atoms contribute an extra p-electron to the delocalised  $\pi$ -system of the graphene lattice.<sup>25–28</sup> In addition, pyrrolic-N atoms are  $sp^2$ -hybridised and are also bonded to two C atoms at the domain edges. Finally, graphitic-N atoms exhibit  $sp^2$ -hybridisation and introduce the remaining two electrons to the delocalised  $\pi$ -system.<sup>25–28</sup> For the oxidised pyridinic-N configurations, the N atoms are bonded to two C atoms and an O atom.<sup>25</sup> Thus, it can be concluded that each of the N-configurations affects the electronic and transport properties of graphene differently. For instance, theoretical studies have indicated that both pyridinic and pyrrolic N-configurations occur at defects, and high concentrations of these configurations induce p-type semiconductor behaviour in nitrogen doped graphene because they withdraw electrons from the graphene film.<sup>29,30</sup> Additionally, the graphitic N-configuration was found to induce n-type conductivity, since one electron becomes engaged in a  $\pi$  bond while the fifth electron forms a partial  $\pi^*$ -bonding state of the conduction band. Each graphitic N-configuration contributes to the  $\pi$  system of the graphene lattice, hence preserving the high mobility of charge carriers in N-doped graphene.<sup>29,30</sup> Contrary to theoretical predictions, experimental work by Lu *et al.* showed that a crossover behaviour from p- to n-type could be observed in N-graphene with an increasing degree of N-doping, especially for graphene films dominated by pyridinic and pyrrolic N-configurations.<sup>31</sup> Schiros and co-workers attributed this crossover behaviour to the hydrogenation of both pyridinic and pyrrolic N

atoms, which then transforms them from p-type to n-type semiconductors.<sup>32</sup>

Similar to N-CNTs, two approaches have been used for the synthesis of N-doped graphene. These include; (1) direct or *in situ* doping during the synthesis of the graphene films and (2) post-doping of the as-synthesized graphene films with a nitrogen source. The latter doping method leads to surface-functionalization of graphene, whereas the former leads to the introduction of heteroatoms into the carbon lattice of graphene, thus resulting in the formation of homogeneously doped graphene films. *In situ* N-doping is the preferred approach and it can be achieved *via* synthesis techniques such as chemical vapour deposition (CVD), segregation growth, solvo-thermal, laser ablation, microwave irradiation, and arc-discharge.<sup>22,33–35</sup> Among the *in situ* synthesis methods, the CVD technique has been extensively studied for the growth of large area N-doped graphene films from gaseous mixtures,<sup>22</sup> liquid organic precursors,<sup>34</sup> and solid precursors.<sup>35</sup> Apart from its easy scalability, CVD enables an easy approach for controlling the nitrogen content in a reaction by changing the flowrate, the ratio between the carbon and nitrogen sources, the growth temperature, as well as the metal catalysts.<sup>22,36,37</sup> For instance, Qu *et al.*<sup>36</sup> showed that growth of N-graphene films on a Ni catalyst at 1000 °C using a 5 : 1  $CH_4/NH_3$  precursor gas mixture produced films consisting mainly of pyridinic and pyrrolic N configurations. On the other hand, Wei and co-workers<sup>22</sup> reported that the graphitic-N configuration was predominately found in N-graphene films grown at 800 °C on a Cu foil using a 1 : 1  $CH_4/NH_3$  gas mixture. Additionally, Luo *et al.*<sup>37</sup> synthesized pyridinic-N rich nitrogen doped graphene films on a Cu foil by using 1 : 1 and 3 : 1  $C_2H_4/NH_3$  mixture at 900 °C.

Interestingly, most reports indicated that successful CVD synthesis of N-doped graphene with varying nitrogen content is dependent on the concentration of the N-precursor material, metal catalyst and the growth temperature. However, the evolution of the N-configurations with time has been little studied. Therefore, this investigation reports a facile method for an in-depth study and understanding of the time-dependent APCVD N-doped graphene film growth using ammonia.



**Scheme 1** Typical configurations of nitrogen atoms in graphene: (1) pyridinic N, (2) substitutional or graphitic N, (3) triple vacancy pyridinic N, (4) pyrrolic N, and (5) oxidized pyridinic-N ( $NO_x$ ).

## 2. Experimental

### 2.1 Starting materials

The reagents used in all experiments were of analytical grade. Acetone (99%, ACE, gold line (CP)) and methanol (MeOH, 99.5%), were bought from Sigma-Aldrich (South Africa). The argon (Ar, 99.9%), methane ( $CH_4$ , 99.98%), ammonia ( $NH_3$ , 10% in Ar) and hydrogen ( $H_2$ , 99.98%) gases were supplied by Afrox, South Africa. Other materials include a copper foil (25  $\mu m$ , 99.98%) from Sigma Aldrich (RSA), poly(methyl methacrylate) (PMMA,  $M_w \sim 999\,000$ , crystalline, Sigma Aldrich), a silicon substrate with 300 nm silicon oxide layer (Sigma-Aldrich), and copper plate and iron wire (University of the Witwatersrand workshop). Distilled water was used throughout the experiments.



## 2.2 Synthesis and transfer of N-doped graphene films

The *in situ* N-doping of graphene films was achieved using APCVD on a copper foil in a quartz tube furnace. All the films were grown using 10 sccm CH<sub>4</sub>, 3 sccm H<sub>2</sub>, 300 sccm Ar, and 5 sccm NH<sub>3</sub>. An electrochemically cleaned<sup>38</sup> Cu foil was placed at the center of the cylindrical quartz tube (100 cm × 20 cm), and the tube was then inserted in a horizontal furnace. The furnace was heated to 1000 °C at a ramping rate of 10 °C min<sup>-1</sup> under atmospheres of H<sub>2</sub> and Ar, and then held at the designated temperature for 30 minutes. The growth of the *in situ* N-doped graphene films was carried out for varying times (2, 5, 10, and 20 min) under 10 sccm CH<sub>4</sub> and 5 sccm NH<sub>3</sub>. The low NH<sub>3</sub> flow rate was chosen to limit Cu corrosion by the NH<sub>3</sub>. In the control experiments, pristine graphene films were grown for the same times (2, 5, 10, and 20 min) using 10 sccm CH<sub>4</sub>. Finally the reactor was rapidly cooled to room temperature by pushing the quartz tube outside the reactor.

After growth, both pristine and N-doped graphene films were then transferred onto the 300 nm SiO<sub>2</sub>/Si substrate using the PMMA-assisted electrochemical delamination method.<sup>38</sup> Initially, a 1 cm × 1 cm square of the as-grown film on Cu was spin coated with a thin layer of PMMA at 2000 rpm for 60 s, after which it was baked at 80 °C for 5 min to ensure good adhesion of the PMMA on the graphene/Cu. From the electrolysis of water, the PMMA/graphene film was then detached from the Cu foil by the generated hydrogen bubbles. After the detachment of the PMMA/graphene film, the floating PMMA/graphene film was transferred onto the SiO<sub>2</sub>/Si substrate. The transferred film was baked at 50 °C for 30 minutes to enable good adherence of PMMA/graphene onto the substrate. Finally, the PMMA was dissolved with warm acetone and the residual PMMA/acetone on the films was removed by washing the films with multiple volumes of methanol and distilled water.

## 2.3 Characterization

The structural characterization of the as-synthesized pristine and N-doped graphene films on 300 nm SiO<sub>2</sub>/Si substrates was studied by Raman spectroscopy. Raman spectra of all films were collected on a Bruker Raman Senterra spectrophotometer (Bruker, South Africa) using a 532 nm excitation laser and at a very low laser power (0.5 mW) to avoid laser-induced heating which can damage the films. Optical imaging was captured by a 50× optical objective lens. The chemical composition of the prepared films was studied by X-ray photoelectron spectroscopy (XPS) at the Thermo Scientific factory in UK. The *ex situ* XPS study was carried out on films grown on Cu foil with a Thermo Escalab 250. The data were referenced to the carbon peak at 284.0 eV (error bar 0.1%). The radiation used was a mono-chromatised aluminium Kα radiation with a 400 μm spot size and a 'pass' energy of 60 eV was used.

## 3. Results and discussion

The structural characterization of the as-grown films was determined by studying their optical images and Raman

spectra; while the degree of N-doping and type of N-configurations were confirmed by studying their XPS spectra.

### 3.1 Microstructural analysis of the films

Optical micrographs (Fig. 1) of N-doped graphene films transferred onto a 300 nm SiO<sub>2</sub>/Si substrate showed large-area, continuous and uniform films. In comparison with their pristine graphene counter-parts (Fig. S1†), N-doped graphene films exhibited regions of multilayers embedded within a uniform and continuous film. The multilayer regions can be ascertained by the dark spots. This is because for pristine graphene films on a 300 nm SiO<sub>2</sub>/Si substrate the thickness can be verified by the colour contrast of the substrate due to the light interference effect.<sup>2,3</sup> Therefore, the darker colour contrast of the substrates indicates a thicker film.

### 3.2 Raman analysis

To study the structural and electronic properties of the as-grown N-graphene films, Raman spectroscopy was used since it is a non-destructive and powerful technique for characterizing carbon materials.<sup>39–46</sup> Fig. 2 shows the Raman spectra of both pristine and N-doped graphene films on a 300 nm SiO<sub>2</sub>/Si substrate synthesized under the same growth conditions. The pristine graphene films (Fig. 2a) exhibited three Raman peaks, which are assigned to D (~1340 cm<sup>-1</sup>), G (~1583 cm<sup>-1</sup>) and 2D (~2675 cm<sup>-1</sup>) bands, respectively.<sup>43,44</sup> Interestingly, the relative intensity of the D band was found to decrease with increasing growth time (2–20 min). This is indicative of an improved quality of the graphene films with prolonged growth time. The Raman spectra of N-doped graphene films (Fig. 2b) showed four peaks, which can be assigned to D (~1350 cm<sup>-1</sup>), G (~1590 cm<sup>-1</sup>), D\* (~1623 cm<sup>-1</sup>), and 2D (~2678 cm<sup>-1</sup>) bands. Furthermore, the pronounced D band relative intensity across the growth regime is an indication of graphene lattice distortion by N atoms. However, it can be seen that the relative D band intensity was not significantly affected by time.

Understanding of the graphene lattice distortion due to N-doping was done by assessing the observed Raman peaks (Fig. 2b). The existence of a strong defect-induced D band (~1350 cm<sup>-1</sup>) in all N-doped graphene Raman spectra is indicative of the successful incorporation of N atoms into the

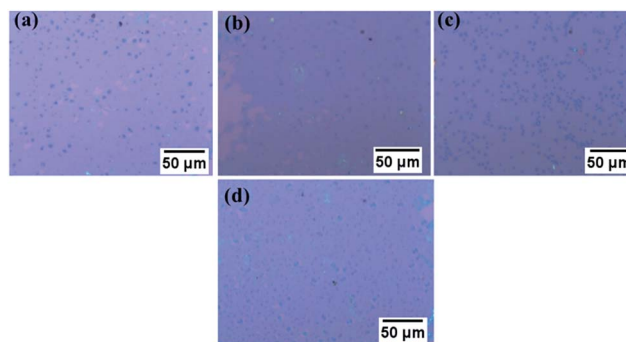


Fig. 1 Optical images of N-doped graphene films grown at (a) 2 min, (b) 5 min, (c) 10 min, and (d) 20 min.



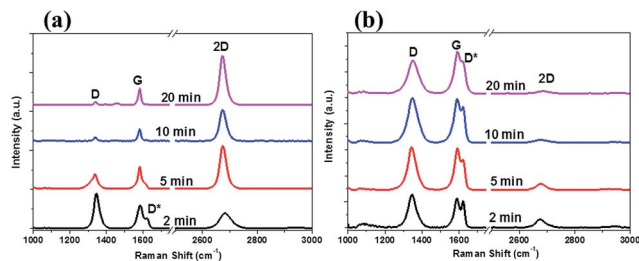


Fig. 2 Raman spectra of pristine (a) and N-doped (b) graphene films grown at varying times.

graphene matrix, hence leading to a broken symmetry of the graphene lattice. The emergence of the D\* band ( $\sim 1623\text{ cm}^{-1}$ ) on the shoulder of the G band is also considered as another Raman feature induced by defects. The D\* band occurs through an intravalley double resonant scattering process, in which the defects provide the missing momentum required to satisfy the resonant process.<sup>39,40,43–45</sup> The relative intensities of these defect-induced peaks indicate the presence of substantial amount of defects; either in the form of in-plane heteroatom substitution, ad atoms, vacancies, and/or grain boundaries/edges. In contrast to both D and D\* bands, the relative intensity of the lattice-defect sensitive 2D band ( $\sim 2678\text{ cm}^{-1}$ ) is significantly suppressed across the growth regime. The 2D band originates from a two-phonon double resonant process and it does not require a defect to fulfill the resonant conditions.<sup>41,47</sup> During N-doping, nitrogen atoms create lattice defects and introduce electron doping; and both of these processes increase the electron/hole scattering rate in N-doped graphene which then leads to the diminished 2D band intensity.

To further understand the degree of lattice distortion and the electronic properties of our films, the positions of the graphitic Raman peak (G band) were studied in detail. These peak positions were observed to have blue shifted by a maximum of  $\sim 9.5\text{ cm}^{-1}$  (red line in Fig. 3a), as compared to their graphene counterparts (black line in Fig. 3a). This blue shifting of the G band could be attributed to the increased electron doping, since this leads to stiffening of the phonons for the G band.<sup>41,46,48</sup> In addition to the position of the G band, the position of the 2D band is another important parameter for an in-depth investigation of the electronic and structural properties of N-doped carbon materials.<sup>40,41</sup> This is because the 2D band position is affected by the modification of the equilibrium

lattice parameter as a result of lattice distortion by nitrogen dopants.<sup>41</sup> Fig. 3b (red line) shows that the 2D band position in N-graphene films are blue shifted by a maximum of  $\sim 12.4\text{ cm}^{-1}$ . The strong blue shift observed in both the G and 2D band positions signifies that not only electron doping contributes to the effect, but also that compressive/tensile strain in the C–C bonds could play an important role in the observed blue shift of both peaks. Earlier theoretical calculations by Allen's group indicated that during N-doping different N-configurations lead to compressive strain on C–C bonds.<sup>49</sup> Their results showed that since pyridinic and pyrrolic bonding configurations have shorter bond lengths ( $\sim 1.32\text{ \AA}$  and  $\sim 1.37\text{ \AA}$  respectively) than that of C–C ( $\sim 1.42\text{ \AA}$ ), then a high concentration of these configurations result in a compressive strain on C–C bonds, thereby leading to a blue shift in the 2D band instead of the well-known red shift. To support the finding by Allen *et al.*, Dettori and co-workers<sup>50</sup> showed that even for defected graphene, defects associated with bond reconstruction do lead to lattice deformation and stress/strain fields. Therefore based on the above analysis, we can ascertain that both electron doping and compressive strain on C–C bonds strongly contribute to the blue shifting of both G and 2D bands.

Commonly, the ratio of the relative intensity of D band to G band ( $I_D/I_G$ ) is used to determine the quality or degree of disorder for as-grown pristine graphene.<sup>39,40</sup> Fig. 4a (black line) shows that the level of disorder in pristine graphene films decreases with increasing growth time. Upon N-doping of graphene films, the  $I_D/I_G$  values (Fig. 4a, red line) are observed to be larger than those of pristine films, and this is due to the structural defects induced by introducing nitrogen dopants into the graphene lattice. Similarly, the  $I_D/I_G$  ratio is seen to decrease with increasing growth time; with the lowest intensity ratio found at 20 min growth time ( $I_D/I_G = 0.87$ ). Ferrari and Robertson<sup>51</sup> attributed this phenomenon to the different arrangements of defects in  $\text{sp}^2$  carbon materials. The high  $I_D/I_G$  ratio values signify the formation of nanocrystalline graphite domains. However, with increasing growth time, these nanocrystallites change until they open up to form a matrix made up of  $\text{sp}^2$  carbon clusters containing low  $\text{sp}^3$  amorphous carbon domains. The loss in the  $\text{sp}^2$  ring in graphite nanocrystallites decreases the intensity of the D band relative to that of the G band; hence leading to the observed decrease in the  $I_D/I_G$  ratio. Therefore, the results indicate fewer lattice distortions are produced with increasing growth time. Recently, Eckmann and

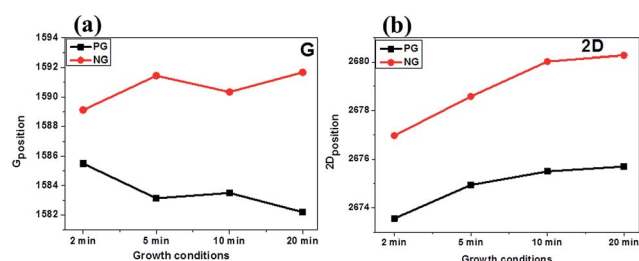


Fig. 3 Peak positions for the G (a) and 2D (b) bands for both pristine and N-doped graphene films.

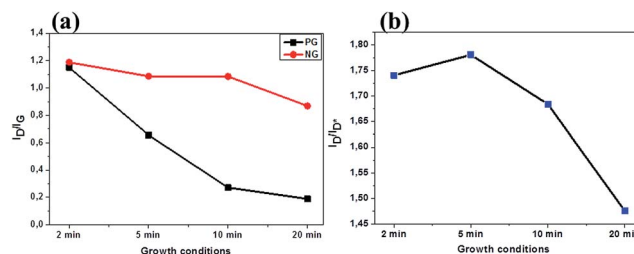


Fig. 4 Evolution of  $I_D/I_G$  (a) with increasing growth time for both pristine and N-doped graphene films and  $I_D/I_{D^*}$  (b) for N-doped graphene films.





co-workers<sup>42</sup> indicated that the nature of defects in graphene films can be determined by Raman spectroscopy by using the intensity ratio of the defect-activated bands ( $I_D/I_{D^*}$ ). They showed that the  $I_D/I_{D^*}$  is at a maximum ( $\sim 13$ ) for  $sp^3$  hybridisation defects at graphene/graphite edges and grains boundaries, and that the value decreases to  $\sim 7$  for on-site/vacancy-like defects. It finally reaches a minimum of  $\sim 3.5$  for defects located at grain/domain boundaries. Therefore, by using the  $I_D/I_{D^*}$  ratio we can determine the nature of defects present in our N-doped graphene films. Fig. 4b shows that the maximum defect-sensitive intensity ratio  $I_D/I_{D^*}$  is  $\sim 1.8$ , which suggests that the N-doped graphene films contain predominately grain/domain boundary defects.

### 3.3 XPS analysis

The XPS analysis was used as a surface sensitive and standard technique for determining the overall degree of N-doping and the different N-configurations in our films. The overall percentage concentrations of the carbon, nitrogen, and oxygen atoms (Fig. 5a) were determined by taking the integrated peak areas of the C1s, N1s, and O1s from the XPS survey spectra. It was seen that the carbon concentration increased (50.6–71.9 at%) while both nitrogen (2.3–2.0 at%) and oxygen (47.0–26.1 at%) concentrations were found to decrease as the growth time increased. The ratio of the integrated peak area of N1s to that of the C1s (*i.e.* N/C ratio) was used to calculate the overall nitrogen content in the films, and this was found to be 4.68%, 3.75%, 3.25%, and 2.84% for the N-graphene films grown at 2, 5, 10, and 20 min, respectively (Fig. 5b). The results indicate that the nitrogen content was strongly dependent on the growth time of the as-synthesized films. The high degree of doping for films grown at 2 min (4.68%) is in agreement with the largest defect intensity ratio ( $I_D/I_G$ ) observed in Fig. 4a. Likewise, the low N-content for films grown at 20 min (2.84%) correlated well with the low  $I_D/I_G$  ratio (0.87). The results indicate that short growth time (2 min) results in the formation of many poorly connected graphene domains, hence permitting a large incorporation of N atoms at the edges or grain boundaries. However, at a longer growth time the graphene domains have started to coalesce into bigger graphene domains, hence making incorporation of more N atoms into the graphene lattice more difficult. Compared to the pristine graphene films (Fig. S2†), the increased oxygen content in the N-doped graphene films indicates a stronger

oxygen adsorption ability on N-graphene films, hence demonstrating a potential application of N-graphene films in fuel cells.<sup>36</sup>

The deconvolution of the N1s XPS spectra was performed to determine the different bonding states (N-configurations) of nitrogen atoms in our N-doped graphene films (Fig. 6 and S3–S5†). Fig. 6 shows that the N1s spectra can be deconvoluted into at least four component peaks attributed to pyridinic-N (397.6–398.1 eV), pyrrolic-N (399.0–399.7 eV), substitutional/graphitic-N (400.6–401.7 eV), and the oxidised pyridinic-N ( $NO_x$ , 402.7–404.6 eV), respectively.<sup>22,25–28,52</sup> The different relative intensities of the N-configurations indicate that the formation of N-graphene films rich in one N-configuration can be controlled by adjusting the growth time. The different chemical environments for the C atoms within the N-doped graphene films were determined by deconvoluting the high-resolution XPS C1s scan, as shown in Fig. 6 and S3–S5.† All C1s XPS spectra exhibited an asymmetrical and tailing peak, which is indicative of different bonding states for C atoms. The main component located at 284.0 eV corresponds to the presence of C atoms in graphite-like  $sp^2$  C–C bonds.<sup>25–27,53</sup> When compared with the peak position of  $sp^2$  C–C in graphite,<sup>53</sup> the main component peak in N-doped graphene films is expected to shift to higher binding energies attributed to the bonding of C atoms (2.55) to the more electronegative N atoms (3.04); this effect is not observed in the C XPS data due to the low N content in the material. Its high intensity indicates that most of the carbon atoms within the N-doped films remain bonded together in a conjugated honeycomb lattice. Two component peaks centred at 285.2–285.7 eV and 286.2–286.9 eV can be assigned to the contribution from N- $sp^2$ -C (graphitic, pyridinic, and/or pyrrolic) and N- $sp^3$ -C (defected  $sp^3$ -C bonds) respectively.<sup>25–27,35,53</sup> Finally, the peak at higher binding energies (288.3–288.5 eV) is attributed to the formation of C–O bonds from the oxygen at the edges of graphene domains.<sup>36,47</sup>

The effect of growth time on the N-configurations was further investigated by determining the % concentrations of all configurations in the N-graphene films, as well as calculating the % amounts of each configuration per N-content (Fig. 7a and b). At 2 min and 5 min growth times the predominant N-configurations are the pyridinic- and pyrrolic-types; which indicate that most of the N atoms are located at the edges or on the defected sites on the graphene domains. Lack of any substitutionally incorporated N atoms confirms the existence of small graphene domains based on the stability for the

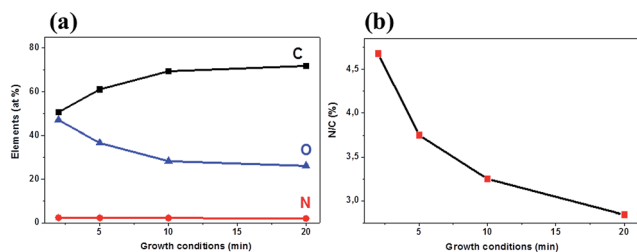


Fig. 5 (a) Atomic composition analysis from the XPS survey spectra and (b) N/C content in N-doped graphene films grown using 10 sccm  $CH_4$  and 5 sccm  $NH_3$ .

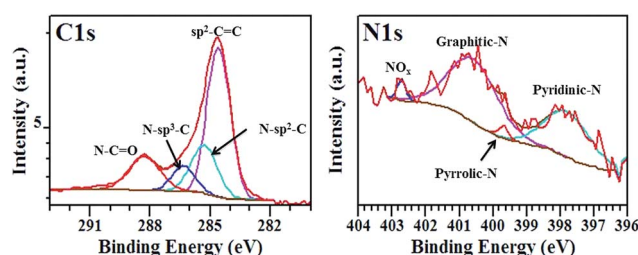


Fig. 6 C1s and N1s core-shell XPS spectra of N-doped graphene films grown at 10 min.



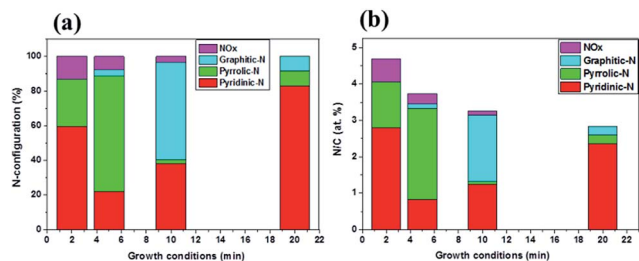
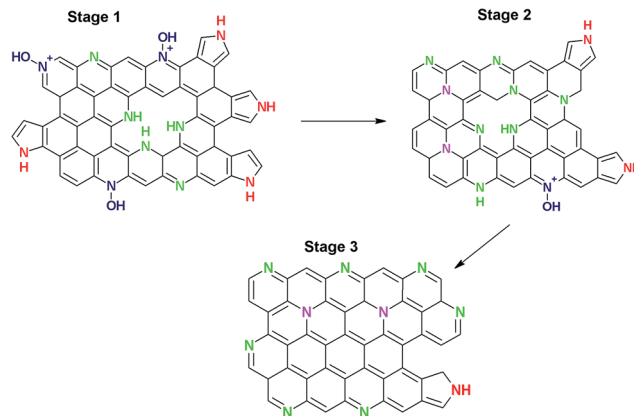


Fig. 7 (a) % N-configurations and (b) contents of pyridinic-N, pyrrolic-N, graphitic-N and NO<sub>x</sub> as a function of growth time.

formation of different bonding states ( $C=C$  (6.24 eV) >  $C-C$  (3.71 eV) >  $C-N$  (2.83 eV));<sup>54</sup> thereby making incorporation of N atoms into the graphene domains difficult. At 10 min growth time, there is almost an equal rate of growth to give both graphitic-N and pyridinic-N bonding states. Finally, at a longer growth time (20 min), the pyridinic-N bonding states reach a maximum of 2.36 at%/total N-content, while growth of both pyrrolic- and graphitic-N was noted. The absence of NO<sub>x</sub> suggests that all the N atoms are perfectly incorporated into the graphene lattice. The observations indicate that prolonged growth time can cause healing of the graphene lattice to form more stable  $sp^2$  bonds, therefore leading to the breakage of the C-N bonds and removal of nitrogen atoms.<sup>52</sup> The results are also in good agreement with theoretical calculations which indicate that N atoms are more thermodynamically stable at graphene edges, and with the pyridinic-type being the most stable.<sup>20–22,51</sup>

### 3.4 Growth mechanism of our samples

Based on the above characterization and analysis, we can, therefore, conclude that the time-dependent growth of N-doped graphene films follows at least a three-stage growth mechanism (Scheme 2). In stage 1 (2 min and 5 min), the N-graphene films contain predominantly pyridinic and pyrrolic-N configurations along with some oxidised pyridinic-N type species. Interestingly, there are little or no graphitic-N type configurations detected, indicating that both pyridinic and pyrrolic-N atoms are found at the graphene domain edges and on defective sites. As a result, high defect density ratio values ( $I_D/I_G = 1.19$  and 1.09 for 2 min and 5 min, respectively) were observed at this stage. The high relative intensity of the pyridinic-N configurations at 2 min growth time could be attributed to the different ways in which the pyridinic-N atoms are placed around the defects (*i.e.* to give mono-, di-, tri- and tetramerized pyridinic defects).<sup>55,56</sup> In stage 2 (10 min), the N-graphene films consisted mainly of graphitic-N type bonding states with minimum amounts of pyridinic-N type atoms. This indicates that there is sufficient time in the doping reaction to permit the successful substitution of C atoms with N atoms, as well as to allow coalescence of graphene domains, as reflected by the slightly lower  $I_D/I_G$  value (1.05). At stage 3 (20 min), the N-graphene films consisted mostly of pyridinic-N, with a small amounts of graphitic and pyrrolic-N atoms and no oxidised pyridinic-N atoms. Unexpectedly, the film exhibited a low defect density ratio ( $I_D/I_G = 0.87$ ), although pyridinic-N type are expected to



Scheme 2 Growth mechanism of N-doped graphene films with increasing growth time (stages 1–3: pyridinic-N, pyrrolic-N, graphitic-N, oxidized pyridinic-N).

increase the defect density. However, this improved quality indicates that prolonged growth time plays a significant role regarding the re-arrangement of pyridinic-N atoms. Since pyridinic-N atoms are bonded to  $sp^2$  hybridized C atoms, we can suggest that at stage 3, most of the pyridinic-N atoms are located at the edges of the graphene domains with some of the N atoms located at defective sites to contribute to the defect density ratio.

## 4. Conclusions

We have successfully synthesized continuous and large area N-doped graphene films using the co-growth of ammonia and methane gases *via* the APCVD technique. We used optical microscopy, Raman spectroscopy and X-ray photoelectron spectroscopy (XPS) to characterize the N-graphene films and to compare them with their pristine graphene counterparts. Nitrogen atoms were incorporated into graphene and the maximum N/C content of 4.68 at% was noted at a short growth time; while a minimum N/C content of 2.84 at% was observed at longer growth times. Furthermore, the type and amount of the N configurations (pyridinic, pyrrolic, graphitic and NO<sub>x</sub>) were found to be time-dependent. At 2 min and 5 min times, pyridinic, pyrrolic-N and NO<sub>x</sub> bonding configurations dominated. A 10 min growth time led to the formation of graphitic-N-rich films, which also contained small amounts of pyrrolic-N and NO<sub>x</sub>. In contrast, the longer growth time (20 min) produced N-graphene films rich in pyridinic-N with some graphitic-N bonding states. The films lacked NO<sub>x</sub> bonding types and few pyrrolic-N configurations were observed.

## Acknowledgements

This work was supported financially by Johnson Matthey Technology Centre (Pretoria) and the University of the Witwatersrand (Postgraduate Merit Award). We would like to acknowledge Dr Riho Green and Dr Richard Smith from Johnson Matthey Technology Centre at Sonning Common, UK, for the XPS analyses.



## References

- 1 K. S. Novoselov, A. K. Geim, S. V. Morozov, D. Jang, Y. Zhang, *et al.*, *Science*, 2004, **306**, 666–669.
- 2 A. K. Geim and K. S. Novoselov, *Nat. Mater.*, 2007, **6**, 183–191.
- 3 A. K. Geim, *Science*, 2009, **324**, 1530–1534.
- 4 A. H. Castro Neto, F. Guinea, N. M. R. Peres, K. S. Novoselov and A. K. Geim, *Rev. Mod. Phys.*, 2009, **81**, 109–162.
- 5 A. A. Balandin, S. Ghosh, W. Bao, *et al.*, *Nano Lett.*, 2008, **8**, 902–907.
- 6 A. A. Balandin, *Nat. Mater.*, 2011, **10**, 569–581.
- 7 D. L. Nika and A. A. Balandin, *J. Phys.: Condens. Matter*, 2012, **24**, 23320–23323.
- 8 S. D. Chen, Y. Zhang, J. Wang, *et al.*, *Sci. China: Phys., Mech. Astron.*, 2013, **56**, 1466–1471.
- 9 K. S. Novoselov, Z. Jiang, Y. Zhang, *et al.*, *Science*, 2007, **315**, 1379–1381.
- 10 X. L. Li, G. L. Zhang, X. D. Bai, X. M. Sun, X. R. Wang, E. Wang, *et al.*, *Nat. Nanotechnol.*, 2008, **3**, 538–542.
- 11 S. S. Li, K. H. Tu, C. C. Lin, C. W. Chen and M. Chhowalla, *ACS Nano*, 2010, **4**, 3169–3174.
- 12 R. Cheng, J. Bai, L. Liao, H. Zhou, Y. Chen, L. Liu, *et al.*, *Proc. Natl. Acad. Sci. U. S. A.*, 2012, **109**, 11588–11592.
- 13 C. Liu, Z. Yu, D. Neff, A. Zhamu and B. Z. Jang, *Nano Lett.*, 2010, **10**, 4863–4868.
- 14 A. L. M. Reddy, A. Srivastava, S. R. Gowda, H. Gullapalli, M. Dubey and P. M. Ajayan, *ACS Nano*, 2010, **4**, 6337–6342.
- 15 F. Schedin, A. K. Geim, S. V. Morozov, E. W. Hill, P. Blake, M. I. Katsnelson, *et al.*, *Nat. Mater.*, 2007, **6**, 652–655.
- 16 G. Giovannetti, P. A. Khomyakov, G. Brocks, V. M. Karpan, J. van den Brink and P. J. Kelly, *Phys. Rev. Lett.*, 2008, **101**, 026803.
- 17 X. C. Dong, D. L. Fu, W. J. Fang, Y. M. Shi, P. Chen and L. J. Li, *Small*, 2009, **5**, 1422–1426.
- 18 A. D. Pablo, *Chem. Phys. Lett.*, 2010, **492**, 251–257.
- 19 P. P. Shinde and V. Kumar, *Phys. Rev. B*, 2011, **84**, 125401.
- 20 M. Deifallah, P. F. McMillan and F. Cora, *J. Phys. Chem. C*, 2008, **112**, 5447–5453.
- 21 L. S. Panchakarla, K. S. Subrahmanyam, S. K. Saha, A. Govindaraj, H. R. Krishnamurthy, U. V. Waghmare, *et al.*, *Adv. Mater.*, 2009, **21**, 4726–4730.
- 22 D. C. Wei, Y. Q. Liu, Y. Wang, H. L. Zhang, L. P. Huang and G. Yu, *Nano Lett.*, 2009, **9**, 1752–1758.
- 23 Y. X. Hou, X. M. Geng, Y. Z. Li, *et al.*, *Sci. China: Phys., Mech. Astron.*, 2011, **54**, 416–419.
- 24 L. Duclaux, *Carbon*, 2002, **40**, 1751–1764.
- 25 C. P. Ewels and M. Glerup, *J. Nanosci. Nanotechnol.*, 2005, **5**, 1345–1363.
- 26 R. J. J. Jansen and H. Vanbakkum, *Carbon*, 1995, **33**, 1021–1027.
- 27 Y. Nakayama, F. Soeda and A. Ishitani, *Carbon*, 1990, **28**, 21–26.
- 28 J. Casanovas, J. M. Ricart, J. Rubio, F. Illas and J. M. Jimenez-Mateos, *J. Am. Chem. Soc.*, 1996, **118**, 8071–8074.
- 29 S. Jalili and R. Vaziri, *Mol. Phys.*, 2011, **109**, 687–694.
- 30 Z. F. Hou, X. L. Wang, T. Ikeda, K. Terakura, M. Oshima and M. Kakimoto, *Phys. Rev. B: Condens. Matter Mater. Phys.*, 2013, **87**, 165401–1654403.
- 31 Y. F. Lu, S. T. Lo, J. C. Lin, W. J. Zhang, J. Y. Lu, F. H. Liu, *et al.*, *ACS Nano*, 2013, **7**, 6522–6532.
- 32 T. Schiros, D. Nordlund, L. Palova, D. Prezzi, L. Y. Zhao, K. S. Kim, *et al.*, *Nano Lett.*, 2012, **12**, 4025–4031.
- 33 Y. Ito, C. Christodoulou, M. V. Nardi, *et al.*, *ACS Nano*, 2014, **8**, 3337–3339.
- 34 Z. Wang, P. Li, Y. Chen, *et al.*, *J. Mater. Chem. C*, 2014, **2**, 7396–7401.
- 35 B. Guo, Q. Liu, E. Chen, *et al.*, *Nano Lett.*, 2010, **10**, 4975–4980.
- 36 L. Qu, Y. Liu, J. B. Baek and L. Dai, *ACS Nano*, 2010, **4**, 1321–1326.
- 37 Z. Luo, S. Lim, Z. Tian, J. Shang, L. Lai, B. MacDonald, *et al.*, *J. Mater. Chem.*, 2011, **21**, 8038–8044.
- 38 Y. Wang, Y. Zheng, X. Xu, E. Dubuisson, Q. Bao, J. Lu and K. P. Loh, *ACS Nano*, 2011, **5**, 9927–9933.
- 39 L. M. Malard, M. A. Pimenta, G. Dresselhaus and M. S. Dresselhaus, *Phys. Rep.*, 2009, **473**, 51–87.
- 40 L. G. Cancado, A. Jorio, E. H. Martins Ferreira, F. Stavale, C. A. Achete, R. B. Capaz, *et al.*, *Nano Lett.*, 2011, **11**, 3190–3196.
- 41 A. Das, S. Pisana, B. Chakraborty, S. Piscanec, S. K. Saha, U. V. Waghmare, *et al.*, *Nat. Nanotechnol.*, 2008, **3**, 210–215.
- 42 A. Eckmann, A. Felten, A. Mishchenko, L. Britnell, R. Krupke, K. S. Novoselov, *et al.*, *Nano Lett.*, 2012, **12**, 3925–3930.
- 43 A. C. Ferrari, *Solid State Commun.*, 2007, **143**, 47–57.
- 44 A. C. Ferrari, J. C. Meyer, V. Scardaci, C. Casiraghi, M. Lazzeri, F. Mauri, *et al.*, *Phys. Rev. Lett.*, 2006, **97**, 187401.
- 45 C. Casiraghi, S. Pisana, K. S. Novoselov, A. K. Geim and A. C. Ferrari, *Appl. Phys. Lett.*, 2007, **91**, 233108.
- 46 Z. H. Ni, T. Yu, Y. H. Lu, Y. Y. Wang, Y. P. Feng and Z. X. Shen, *ACS Nano*, 2008, **2**, 2301–2305.
- 47 P. Venezuela, M. Lazzeri and F. Mauri, *Phys. Rev. B*, 2011, **84**, 035433.
- 48 Z. Zafar, Z. H. Ni, X. Wu, Z. X. Shi, H. Y. Nan, J. Ba, *et al.*, *Carbon*, 2013, **61**, 57–62.
- 49 F. H. Allen, O. Kennard, D. G. Watson, L. Brammer, A. G. Orpen and R. Taylor, *J. Chem. Soc., Perkin Trans. 2*, 1987, **12**, S1–S19.
- 50 R. Dettori, E. Cadelano and L. Colombo, *J. Phys.: Condens. Matter*, 2012, **24**, 104020.
- 51 A. C. Ferrari and J. Robertson, *Phys. Rev. B*, 2000, **61**, 14095–14107.
- 52 R. T. Lv, Q. Li, A. R. Botello-Méndez, T. Hayashi, B. Wang, A. Berkdemir, *et al.*, *Sci. Rep.*, 2012, **2**, 586.
- 53 H. Wang, T. Maiyalagan and X. Wang, *ACS Catal.*, 2012, **2**, 781–794.
- 54 X. Ding, *J. Mater. Chem.*, 2014, **2**, 3717–3722.
- 55 C. K. Lin, *J. Phys. Chem. C*, 2015, **119**, 27131–27144.
- 56 F. Joucken, Y. Tison, J. Lagoute, J. Dumont, D. Cabosart, B. Zheng, *et al.*, *Phys. Rev. B*, 2012, **85**, 161408.

